Evaluation of a graphene-covered dielectric microtube as a refractive-index sensor in the terahertz range

Elena A Velichko

Institute of Radio-Physics and Electronics NASU, Kharkiv 61085, Ukraine

E-mail: elena.vel80@gmail.com

CrossMark

Abstract

We studied the scattering and absorption of the H-polarized plane wave by a graphene-covered circular dielectric cylinder and a hollow tube with a graphene cover on the outer boundary in the terahertz range. The analytical solution of the wave-scattering problem was based on the Maxwell equations and the use of the separation of variables in the polar coordinates. We assumed the resistive boundary conditions on the zero-thickness graphene cover where the graphene electron conductivity was included as a parameter and was determined from the Kubo formalism. The computed spectra of the total scattering cross section and the absorption cross section displayed several types of resonances: the localized-surface-plasmon (LSP) resonances of the graphene cover and the resonances on the whispering-gallery modes of a dielectric cylinder or dielectric tube. The computed data can be useful for the design of graphene-based sensors of the changes in the refractive index of the host medium. For this purpose, the sensitivities and the figure-of-merit values of the LSP resonances were computed; their comparison demonstrated advantages of a thin-tube configuration.

Keywords: terahertz wave, scattering, graphene, plasmon, sensitivity, figure of merit

(Some figures may appear in colour only in the online journal)

1. Introduction

Being famous today as a promising new material, graphene is a single-atom layer of carbon. It has remarkable electromagnetic properties as a zero-band-gap semiconductor with conductivity tuned either by electrostatic or by magnetostatic gating. Besides, it can support surface plasmon (SP) waves with complex-valued propagation constants that are lossy slow waves with fields concentrated at the graphene layer. The existence of these SP waves leads to the appearance of sharp resonances on the localized SP (LSP) standing-wave modes on the patterned graphene samples at low and medium terahertz (THz) frequencies. Such properties make graphene attractive for the development of various tunable nanoelectronic devices—see [1–8]. Most of them are designed as planar ultrathin structures, however, today graphene layers, conformal to the curved microscale surfaces, also attract the attention of researchers [9–11].

The presence of SP waves points out a certain similarity between electromagnetic properties of graphene in the THz range and a noble-metal layer in the optical range. Therefore, one can expect to find further similarities in the scattering behavior and in the corresponding spectral ranges between graphene-covered and metal-covered dielectric cylinders. Elongated gold and silver nanorods and nanotubes are known to support optical LSP modes of several types and symmetries that are responsible for the resonance effects in light scattering and absorption. Each of them can be used, in principle, for the sensing of small changes in the host-medium refractive index caused by the change in concentration of an analyzed substance. The efficiency of such a sensor depends, however, on the type of resonance, its sharpness (i.e., quality factor), and its coupling to the incident illumination [12]. Experimental observations have shown that, in the dense random bed-of-pins nanosensor configurations, the transversal LSP resonances on noble-metal nanotubes dominate over the
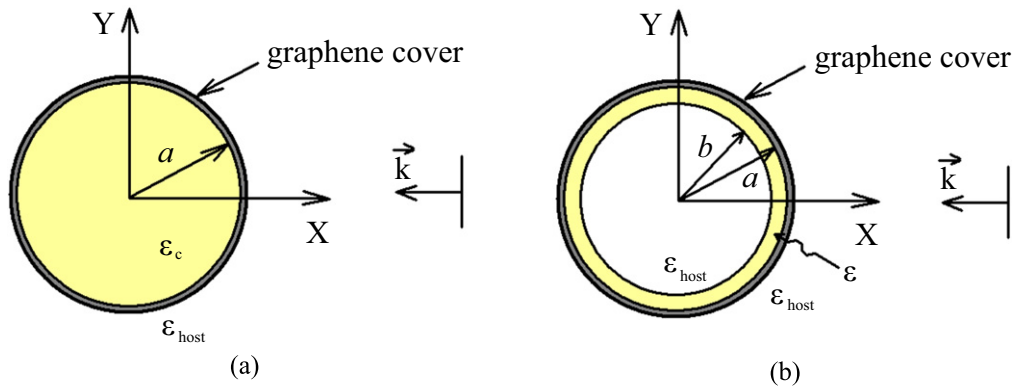
Figure 1. Cross-sectional geometry of (a) a dielectric circular cylinder, (b) a tube covered with a graphene layer.

longitudinal ones [13, 14]. Therefore, the scattering characteristics of nanorods and nanotubes were studied in many papers using the two-dimensional (2D) formulations. In particular, in [15, 16], we presented a study of the bulk refractive-index sensitivities and figure-of-merit (FOM) values of the transversal hybrid-type LSP resonances on silver and gold nanotubes, respectively.

The similarity mentioned above suggests that a graphene-covered microsized tube can also be used as a sensor of the refractive index, however, in the THz range, instead of the optical frequencies. Therefore, estimations of the sensitivity and the FOM of such a sensor are necessary. From a general point of view, the best sensitivity can be expected from a bare graphene tube, however, such a configuration is not practical. For mechanical rigidity, graphene normally is deposited on some supporting structure, which, in our case, can be either a dielectric rod or a dielectric tube. Thus, in this work, we studied the scattering and absorption of electromagnetic waves by a solid circular dielectric cylinder and a hollow circular dielectric tube with a graphene cover attached to the outer surface. For this purpose, we combined the Maxwell boundary-value problem with a phenomenological model of graphene conductivity. Here, we considered the graphene as a zero-thickness layer with a complex-valued surface conductivity, which is determined by the chemical potential, frequency, room temperature, and the relaxation time according to the Kubo formula.

Similar graphene-on-rod configurations were considered recently in [9–11]. The paper [9] concentrated on the study of the natural modes using commercial software, the accuracy of which is far from clear. Besides, the role of the natural-mode resonances in the modification of the scattering and absorption remained not analyzed. These resonances were studied for the graphene-covered dielectric rods in [10, 11] and the metallic rods in [11]. The rod radius was taken as several dozen nanometers that shifted the associated LSP resonances to the upper end of the THz range. Still, no analysis of a graphene-on-tube configuration was presented so far, and the sensor characteristics remain not quantified.

In contrast to [9] and other studies using the brute-force-based commercial software to analyze electromagnetic fields in simple geometries, we fully exploit the advantages of the

circular shape of the studied sensor and use the classical method of separation of variables. Then, the scattered field is found analytically in the form of a rapidly converging Fourier series in the polar coordinates with known coefficients depending on the cylindrical functions.

Therefore, the associated sensor characteristics can be computed with accuracy to machine precision, even in the vicinity of sharp resonances on the high-quality natural modes. It is worth recalling that numerical codes based on the finite-element and finite-difference in time domain (FDTD) methods fail to provide reasonable accuracy in such resonances—see [17–19] for the discussion of that inadequacy. Besides, the analytical solution can be computed very quickly in terms of processor time. This makes it possible to compute the finest details of the frequency dependences with excellent accuracy of the desired number of correct digits in extremely wide ranges (namely, from 1 GHz to 10 THz) in seconds, even with a moderate desktop computer. Such a performance is unthinkable with FDTD codes that need many dozens of hours of computing. Even worse—FDTD codes involve the meshing of the spatial domain, and the mesh must be adapted to the wavelength; therefore, the accuracy deteriorates quickly with the frequency if the mesh is kept the same—see the plots in figure 4 of [5] as an example of this failure.

2. Scattering problem solution

The scattering problems are formulated as follows. Consider a circular dielectric cylinder of radius a with a graphene cover, a circular dielectric tube of inner radius b, and outer radius a with a circular graphene layer placed on the outer surface of the tube (see figures 1(a), (b), respectively). The relative dielectric permittivities of the host medium and the substrate are denoted as ϵ_{host} and ε_c, respectively. The polar coordinates (r, φ, z) are introduced coaxially with the scatterer, and the incident time-harmonic $[\sim \exp(+i\omega t)]$ H-polarized plane wave propagates opposite the x-axis.

We assume that these circular objects are infinite along the z-axis and the electromagnetic field does not depend on z. In either case, we obtain a 2D scattering problem in which we have to find a scalar function $H_z(r, \varphi)$, which is the magnetic

field z component in the coaxial polar coordinates (r, φ, z). It must satisfy the Helmholtz equation with different wave numbers inside and outside the dielectric domains, the radiation condition on infinity, and the condition of local finiteness of power. On the outer boundary, where the graphene cover is located ($r = a$), the following resistive-type boundary conditions are imposed [5–8, 20]:

$$(1/2)(E_\varphi^+ + E_\varphi^-) = Z \, \vec{n} \times (H_z^+ - H_z^-), \qquad E_\varphi^+ = E_\varphi^-. \tag{1}$$

Here, $\vec{n}$ is the unit vector normal to the cylinder boundary, $Z = 1/\sigma$ is the surface impedance of a graphene monolayer, and σ is the graphene surface electron conductivity, which can be assumed isotropic if the wavelength is much larger than the graphene nanoscale fine structure. Note that, if $Z = 0$, then (1) transforms to a perfectly electrically conducting (PEC) boundary condition $E_\varphi^+ = E_\varphi^- = 0$, and, if $|Z| = \infty$, it transforms to conventional dielectric-interface conditions, $H_z^+ = H_z^-$, $E_\varphi^+ = E_\varphi^-$. In the case of a tube, the tangential field components are additionally requested to be continuous across the inner boundary $r = b$. These conditions complete the formulation and guarantee the solution uniqueness.

We would like to emphasize that the concentric-circular configuration of the studied sensor model makes use of low-accuracy numerical algorithms, such as the FDTD ones and frequency-domain finite-element ones not justified. Instead, classical separation of variables (first done in 1881 by Strutt, later known as Lord Rayleigh [21]) leads to an exact analytical solution in the form of a rapidly convergent series with easily computable coefficients. Thus, any problems of bad convergence or numerical artifacts are avoided completely.

In our study, we followed the notations of Wait [22] and presented the total-field function as a sum of the incident electromagnetic field $H_z^{inc}(r, \varphi) = \exp(\gamma x)$, where $x = r \cos \varphi$, $\gamma = ik\sqrt{\epsilon_{host}}$ is the propagation constant in the outer medium ($k = \omega/c$ being the free-space wave number and c being the free-space light velocity), and the scattered field. Furthermore, we expanded the fields into infinite Fourier series, taking into account the dielectric properties of the corresponding materials and used the set of the boundary conditions to determine the expansion coefficients explicitly.

In the case of the graphene-covered circular dielectric cylinder shown in figure 1(a), the following expressions were obtained:

$$H(r, \varphi) = \sum_{m=0}^{\infty} \delta_m \begin{Bmatrix} [I_m(\gamma r) + R_m K_m(\gamma r)], & r > a \\ T_m I_m(\gamma_c r), & r < a \end{Bmatrix} \cos m\varphi, \tag{2}$$

$$R_m = [I_m' \tilde{I}_m' + (Z/Z_0)(n_c I_m' \tilde{I}_m - n_{host} I_m \tilde{I}_m')] \Delta_m^{-1}, \tag{3}$$

$$T_m = n_c \left\{ \frac{I_m'}{\tilde{I}_m'} - \frac{K_m'}{\tilde{I}_m'} \left[I_m' + \frac{Z}{Z_0}(n_c I_m' \tilde{I}_m - n_{host} I_m \tilde{I}_m') \right] \Delta_m^{-1} \right\}, \tag{4}$$

$$\Delta_m = (Z/Z_0)(n K_m \tilde{I}_m' - n_c K_m' \tilde{I}_m) - K_m', \tag{5}$$

where the following notations are used: $Z_0 = \sqrt{\mu_0/\varepsilon_0}$ is the free-space impedance, $\gamma = ikn_{host}$, $\gamma_c = ikn_c$, $n_{host} = \sqrt{\epsilon_{host}}$, $n_c = \sqrt{\varepsilon_c}$, $I_m = I_m(\gamma a)$, and $\tilde{I}_m = I_m(\gamma_c a)$ are the modified Bessel functions, $K_m = K_m(\gamma a)$ are the Macdonald functions, the prime means differentiation in the argument, and δ_m is 1 if $m = 0$ and 2, otherwise. Note that equations (2)–(5) are fully equivalent to the similar equations of [10, 11] where the Fourier expansions involved conventional cylindrical functions of the arguments ka and $kn_c a$.

The optical characteristics, which we were interested in, are the total scattering cross section (TSCS) and the extinction cross section (ECS), calculated using the following expressions, respectively:

$$\sigma_{sc} = \frac{\pi^2}{kn_{host}} \sum_{m=0}^{\infty} \delta_m \, |R_m|^2, \tag{6}$$

$$\sigma_{ext} = \frac{2\pi}{kn_{host}} \text{Im} \sum_{m=0}^{\infty} \delta_m R_m \cos(m\varphi). \tag{7}$$

Besides them, we also computed the absorption cross section (ACS), which can be found, according to the optical theorem, as the difference between ECS and TSCS.

In the case of the graphene-covered circular dielectric tube shown in figure 1(b), the coefficients R_m take a more complicated form than (3) (not shown here), involving the functions $I_m(\gamma b)$, $I_m(\gamma_c b)$, $K_m(\gamma b)$, and $K_m(\gamma_c b)$. In computations, we truncated the series at the finite value of $M = ka\nu + 10$ that guaranteed the accuracy of five digits in the near field provided that ν was the largest of n_c and n_{host}.

3. Graphene conductivity

Graphene surface conductivity is commonly determined from the so-called Kubo formalism and is expressed as a sum of intraband (σ_{intra}) and interband (σ_{inter}) contributions given as follows [5, 6]:

$$\begin{aligned} \sigma = \sigma_{intra} + \sigma_{inter} &= \frac{ie^2 k_B T}{\pi \hbar^2 (\omega + i/\tau)} \\ &\times \left[\frac{\mu_c}{k_B T} + 2 \ln \left(e^{-\frac{\mu_c}{k_B T}} + 1 \right) \right] + \frac{ie^2(\omega + i/\tau)}{\pi \hbar^2} \\ &\times \int_0^{\infty} \frac{f_d(-\delta) - f_d(\delta)}{(\omega + i/\tau)^2 - 4(\delta/\hbar)^2} d\delta, \end{aligned} \tag{8}$$

where e is the electron charge, k_B is the Boltzman constant, T is the temperature, $\hbar$ is the reduced Planck constant, ω is the angular frequency, τ is the electron relaxation time, μ_c is the chemical potential, and f_d is the Fermi–Dirac distribution function.

In figure 2, we present the frequency dependences of the real and imaginary parts of the surface impedance of a graphene monolayer for four different values of the chemical potential at room temperature. Note the positive values of Im Z (for the selected time dependence, this corresponds to the inductive impedance), which are responsible for the existence of the SP guided waves on a sheet of graphene in the case of
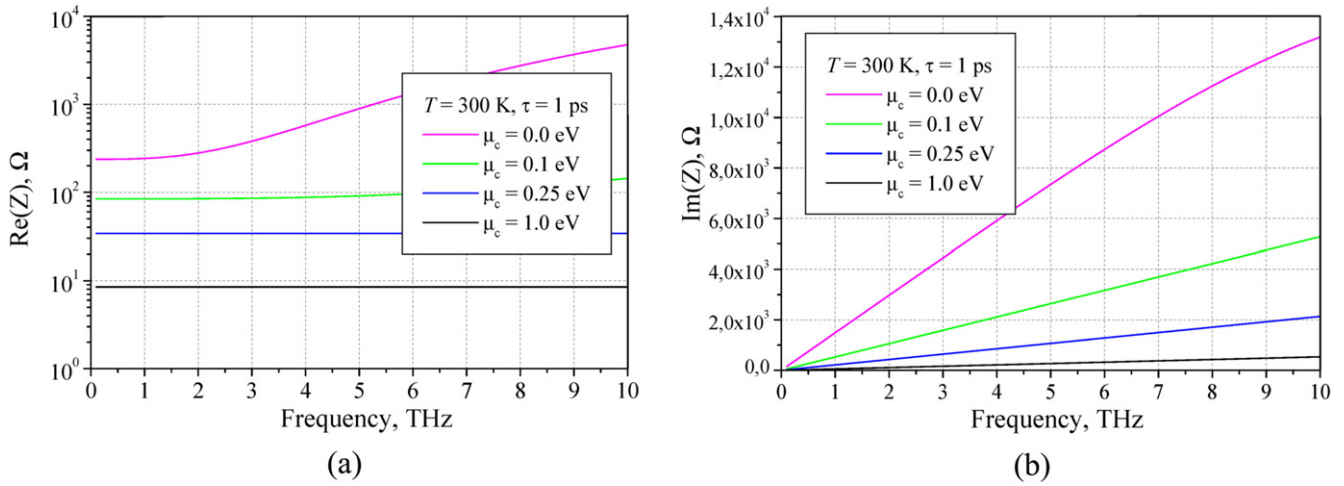
Figure 2. (a) Real, (b) imaginary parts of the graphene complex surface impedance $Z = 1/\sigma$ in the THz range calculated at a room temperature of $T = 300$ K and $\tau = 1$ ps with different values of the chemical potential μ_c.
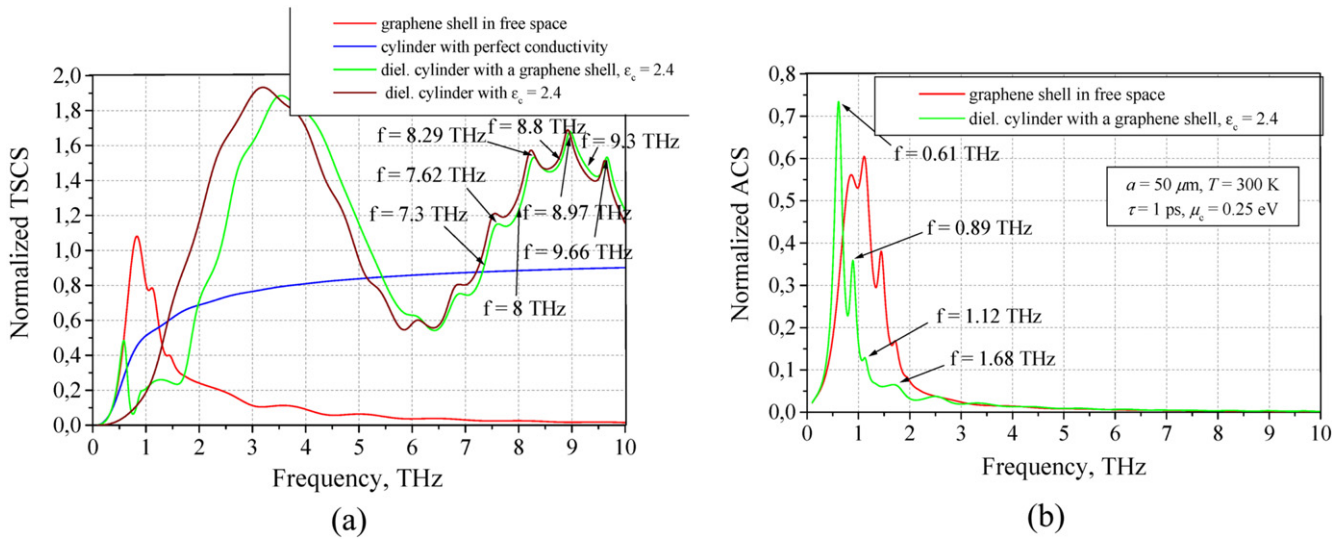

Figure 3. Comparison of the (a) normalized TSCSs, (b) normalized ACSs versus the frequency for various circular cylindrical scatterers with radii of $a = 50\ \mu$m in free space.

H polarization. As can be seen, an increase in the chemical potential up-shifts the frequencies where graphene presents large inductive behavior and leads to the lower losses.

4. Numerical results: graphene-covered dielectric cylinder

Figure 3 shows the plots of the normalized TSCS and ACS versus the frequency for a solid circular dielectric cylinder with a radius of $50\ \mu$m and the relative dielectric constant $\varepsilon_c = 2.4$ (silicon dioxide as an example of a glasslike material) with and without a graphene shell. Such a radius was selected in order to shift the lowest LSP peak to the frequencies around 1 THz and even to lower frequencies where available circuit components and receivers are cheaper and less lossy.

For a better understanding of the resonances, we added the curves corresponding to a free-standing circular shell of graphene and to a PEC cylinder of the same radius. Note that the cross sections are normalized by 4a, which is the limiting value of the TSCS of a PEC cylinder in the case of infinitely high frequencies.

As one can see, the spectrum of the TSCS of an uncovered (i.e., without graphene) lossless dielectric cylinder displays two types of features: broad large-scale oscillations caused by the interference of waves reflected from the front of the cylinder and from its back along the symmetry line, and much sharper small spikes appearing at higher frequencies in an almost periodic manner. The spikes are the resonances on the whispering-gallery modes (WGMs) of the dielectric cylinder—their Q factors grow up exponentially with frequency, and, hence, they are more visible at higher frequencies. Their periodicity in frequency approximately corresponds to the circumference of the cylinder being an
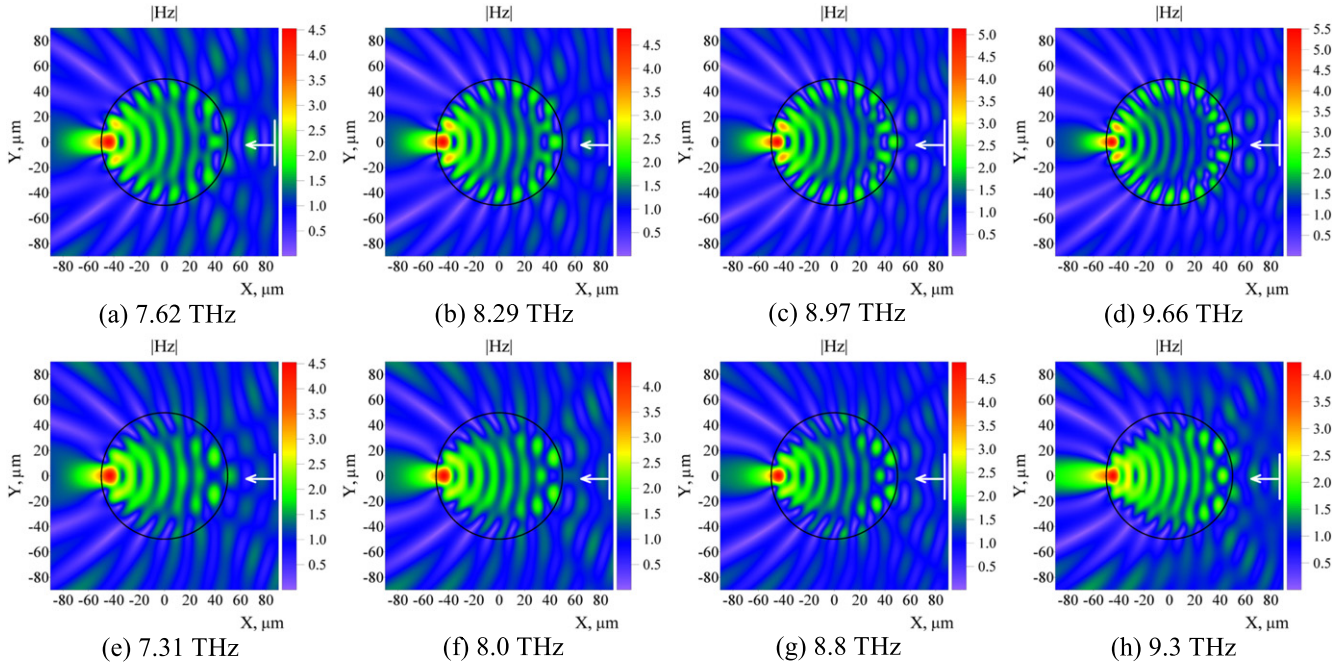
Figure 4. The upper line is for the magnetic field patterns for a dielectric cylinder with a graphene shell at the frequencies of the WGM resonances marked in figure 3(a): (a) $H_{9,1}$, (b) $H_{10,1}$, (c) $H_{11,1}$, (d) $H_{12,1}$. The lower line is for the field patterns at frequencies between the WGM resonances.
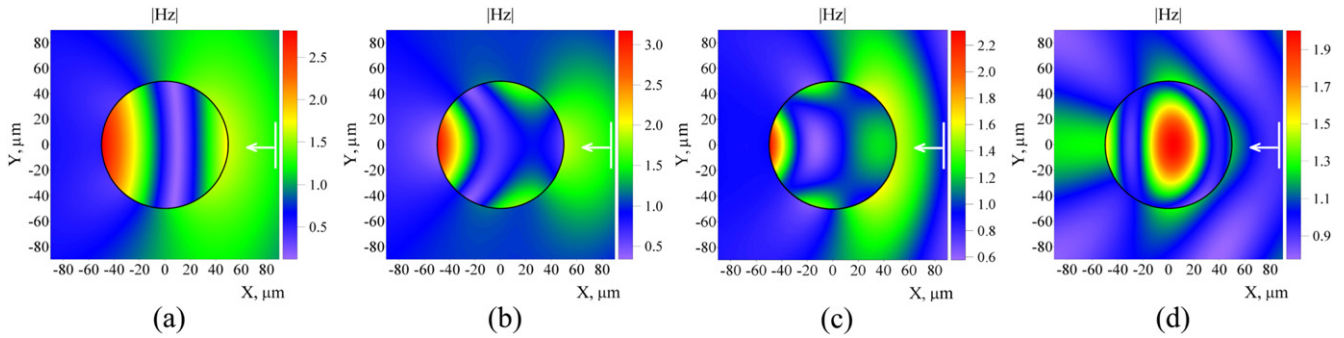

Figure 5. In-resonance magnetic field patterns for a dielectric cylinder with a graphene shell at the frequencies of the LSP resonances marked in figure 3(b): (a) P_1, 0.61 THz, (b) P_2, 0.89 THz, (c) P_3, 1.12 THz, (d) P_4-$H_{0,1}$, 1.68 THz.

integer number of the wavelengths in the material. The WGM spikes keep their locations for the graphene-covered dielectric cylinder, however, they are slightly degraded because of additional losses brought by the graphene cover.

In figure 4, the spatial distributions of the magnetic field magnitude $|H_z|$ for a circular dielectric cylinder with a graphene cover are presented. They were calculated at the WGM resonance wavelengths corresponding to the peaks on the green curve in figure 3(b) indicated by the arrows (upper row) and between the resonances (lower row).

The WGMs are clearly identified by the corresponding number ($2m$) of the field hot spots along the inner side of the circular resonator contour. These spots are absent in the field patterns computed between the peaks. The dominating feature is, however, a very intensive nanoscale spot at the backside of the dielectric cylinder. This spot is commonly known as a 'nanojet' and is explained by the geometrical optics

mechanism of focusing spoiled by the aberrations. Note that the nanojet gets more tightly concentrated at higher frequencies.

Still, there exist the other types of resonances, which are absent for the uncovered dielectric cylinder. This is the LSP resonances of the graphene shell appearing in the lower-frequency part of the THz range in figure 3(a). As our dielectric is assumed lossless, LSPs are solely responsible for the peaks in absorption. In figure 5, we show the near-field patterns calculated at the resonance wavelengths corresponding to the peaks on the green curve in figure 3(b), indicated by the arrows. They allow us to see that the lowest, in frequency, resonances are associated with the LSP modes P_m of the first to the third orders (dipole, quadrupole, and hexapole) as certified by the corresponding number of hot spots on the graphene shell. The fourth is a resonance on the hybrid mode P_4-H_{01}. This hybridization is revealed by the presence of the
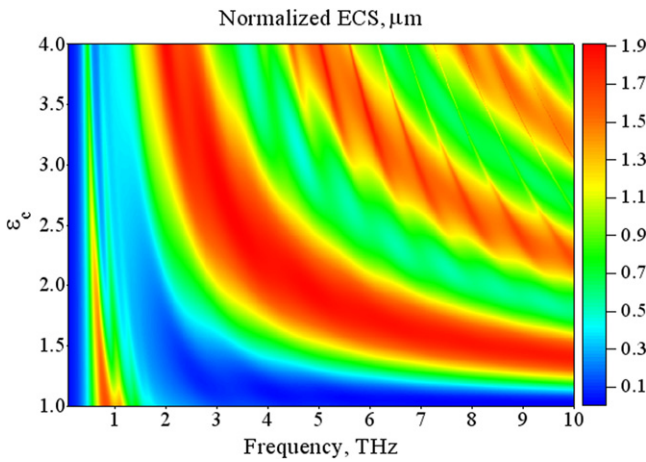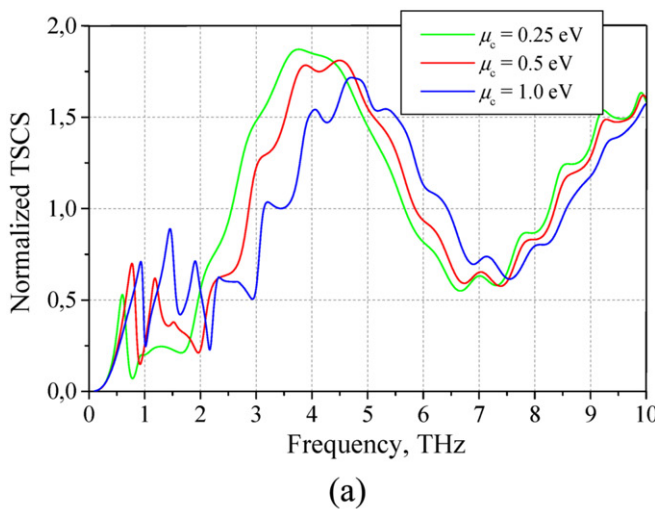
Normalized ECS, μm

Figure 6. A map of the ECS as a function of the frequency and the permittivity for a dielectric cylinder with a radius of $a = 50$ μm covered with a graphene shell. The other parameters are the same as in figure 3.

intensive hot spot in the center of the cylinder together with the smaller hot spots at its boundary.

As one can see, a graphene-covered dielectric cylinder is a complicated open resonator. Therefore, the choice of dielectric material is important. In figure 6, we present the color map of the normalized ECS (which is the sum of the TSCS and the ACS) of the same 50 μm dielectric cylinder with a graphene cover as a function of two variables: the wavelength and the relative dielectric permittivity of the cylinder.

The dielectric-cylinder resonances show up as bright red 'ridges' having the shape of hyperbolas on the wavelength-ε plane. These broad ridges are overlapped with a large number of narrower hyperbolic-shaped ridges corresponding to the WGMs. In contrast, the LSP resonances are seen as a few almost vertical narrow ridges in the low-frequency part of the mentioned plane. It is clear from that map that, for the sensing applications, it is more advantageous to use the lowest-order LSP resonance on a graphene-covered dielectric cylinder with a low permittivity because, then, the dielectric-cylinder

resonances are shifted far enough to the high frequencies. Silicon dioxide can be a good compromise in view of its durability, however, materials with smaller ε_c are even better.

To highlight the tunability of a graphene-assisted scatterer, figure 7 shows the plots of the normalized TSCS and ACS versus the frequency for the same 50 μm circular dielectric cylinder with a graphene cover for three different values of chemical potential μ_c. As one can see, with increasing chemical potential, the plasmon resonances are shifted to higher frequencies, while the WGM peaks remain at their positions. Low-order resonances in the cylinder, located between the LSP and the WGM peaks, show greater dependence on the graphene properties. This is probably because of the hybridization between the two mentioned types of natural modes in the range of 'intermediate' frequencies, similar to the optical dielectric and metal–dielectric concentric circular resonators [15, 16, 23] and to the clusters of optically coupled circular resonators [24].

Finally, as we were interested in the host-medium refractive-index sensing, we calculated the spectra of the ECS of a graphene-covered dielectric cylinder placed into different host media with two different values of the chemical potential —see figure 8. As visible, the LSP resonances on the cylinder are rather insensitive to the changes in n_{host} that make such a configuration not practical. Additionally, larger values of the chemical potential entail smaller graphene impedances (see figure 2) that make it less transparent. This leads to a more pronounced split of the LSP resonances of different azimuthal orders (see panel (b)).

5. Numerical results: graphene-covered dielectric tube

The low sensitivity of the dielectric-rod-based graphene-covered configuration suggests that improvement can be achieved by replacing a rod with a hollow tube (as mentioned above, and the complete elimination of the dielectric substrate
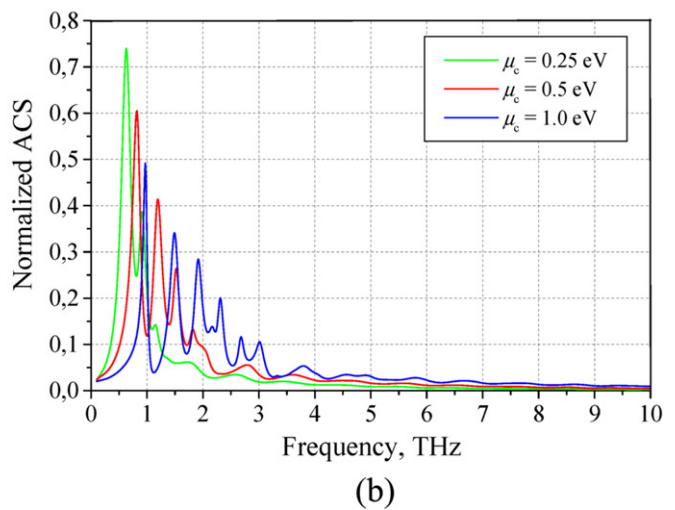

(a)

(b)

Figure 7. The same as in figure 3 for a dielectric cylinder with a radius of $a = 50$ μm and permittivity of $c_c = 2.4$ with a graphene shell and different values of chemical potential μ_c. The other parameters are the same as in figure 3.
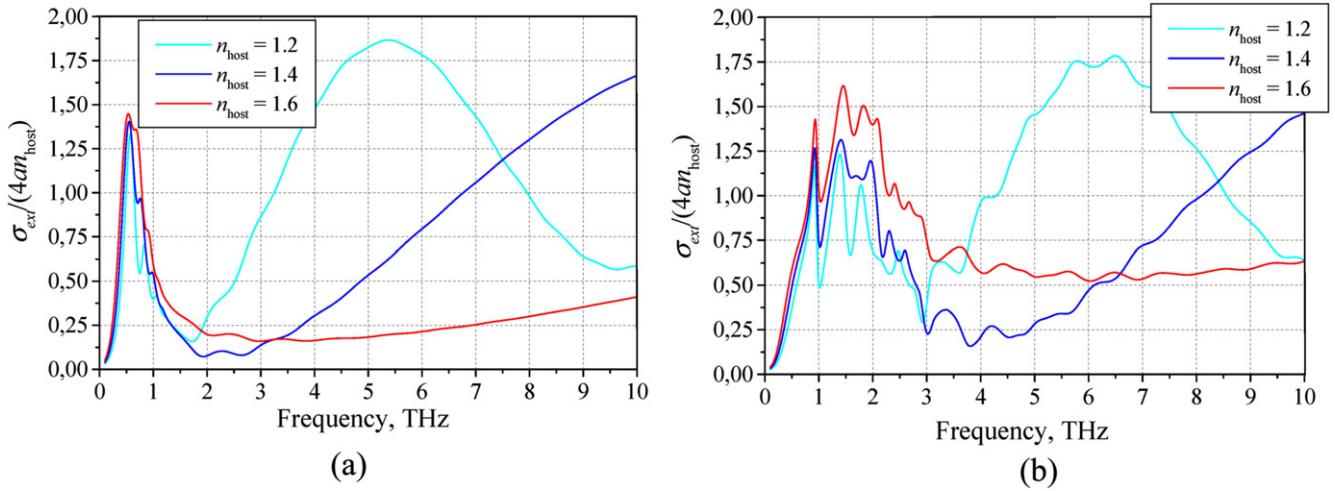
Figure 8. The spectra of the normalized ECS for different values of the host-medium refractive index n_{host}. The dielectric cylinder of the dielectric permittivity $\varepsilon_c = 2.4$ and $a = 50\,\mu$m with a graphene cover for (a) $\mu_c = 0.25$ eV, (b) $\mu_c = 1.0$ eV.
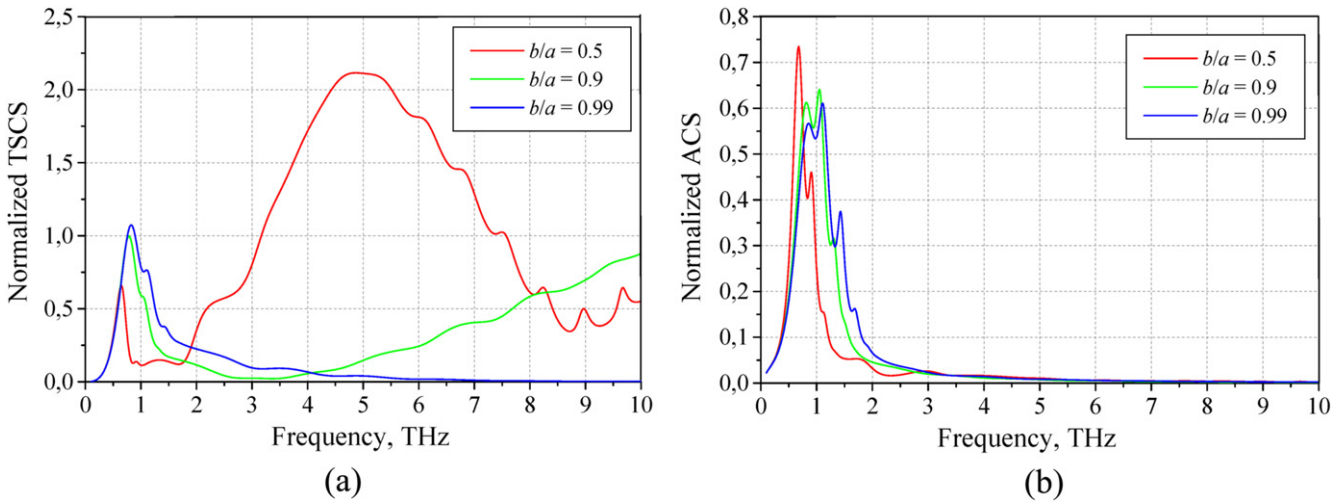

Figure 9. The normalized (a) TSCS, (b) ACS versus the frequency for a dielectric tube with a graphene cover for various ratios of the inner and outer radii. Calculations are made at a room temperature of $T = 300$ K, $\tau = 1$ ps, chemical potential of $\mu_c = 0.25$ eV, and tube permittivity of $\varepsilon_c = 2.4$. The other parameters are the same as in figure 3.

is not practical). Indeed, figure 9 shows the plots of the normalized, by $4a$, TSCS and ACS versus the frequency for a dielectric tube with a graphene cover for several ratios of the inner and outer radii. The outer radius of the dielectric tube was fixed at $50\,\mu$m, its relative dielectric constant was taken as $\varepsilon_c = 2.4$, and the free space was assumed inside and outside the tube.

As one can see, if the tube is thick as $b/a = 0.5$, the spectra of the TSCS and the ACS display the same two types of resonances as discussed in detail for the solid rod covered with graphene. One of them is the LSP resonances appearing at the lower-frequency part of the THz range, both in the scattering and in the absorption. The other type is the resonances on the WGMs of the dielectric tube, better visible at higher frequencies. The most interesting point is that the WGM resonances shift away from the THz range (to higher frequencies) if the tube becomes thinner than 10% of the tube's outer radius. As the dielectric material of the tube is

assumed lossless, only the LSP modes are responsible for the resonance peaks in the absorption.

In figure 10, we present the color map of the ECS as a function of the frequency and the varying ratio of the tube thickness (a), (b) to the outer radii a. Here, a hollow graphene-covered dielectric microtube was placed in air, and the tube permittivity was $\varepsilon_c = 2.4$.

As one can see, replacing a solid dielectric cylinder with a thin dielectric tube had basically the same effect as making the dielectric permittivity of the cylinder much smaller than it is typical for glasslike materials (compare the maps in figures 6, 10). Thus, the tube-based resonance structure appears more attractive than the rod-based one.

Keeping in mind the sensing applications, we computed the ECS spectra of the graphene-covered dielectric tubes in the medium with several values of refractive index n_{host}, both inside and outside the tube. The corresponding results are demonstrated in figure 11. For comparison, two values of the
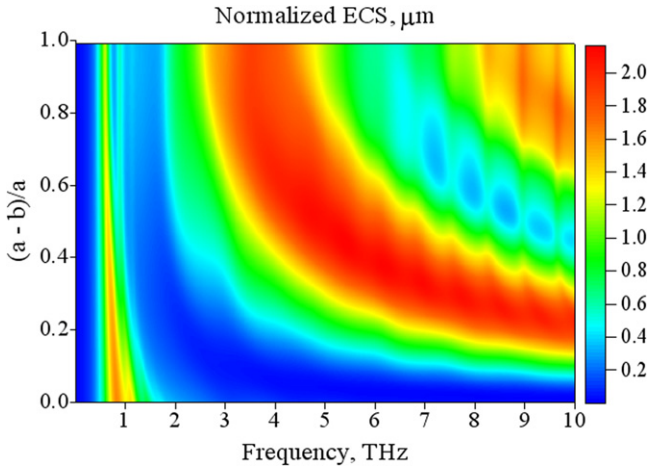
Figure 10. A map of the ECS as a function of the frequency and the ratio of the tube thickness to the outer radii for a circular dielectric tube covered with a graphene layer. The other parameters are the same as in figure 8.

radii ratio b/a were considered, 0.5 (thick-walled tube) and 0.99 (thin-walled tube). As visible, with the growth of the host-medium refractive index, the LSP resonance peaks shifted down in frequency; this shift was considerably larger for a thin-walled tube—see panel (d).

The plots in figure 12 present similar dependences, however, for a larger value of the chemical potential, $\mu_c = 1.0$ eV. As already mentioned, this corresponds to a less transparent graphene layer than in figure 11.

Thus, the LSP-resonance wavelengths of the tube-based composite scatterer are indeed well sensitive to the refractive-index change. As a more complete illustration of the THz response of a dielectric tube with a graphene cover, in figure 13, we present the color maps of the ECS as a function of the frequency and the host-medium refractive index.

Here, a hollow dielectric tube with a graphene shell was immersed into and was filled in with an analyte medium of a varying refractive index. The maps demonstrate the
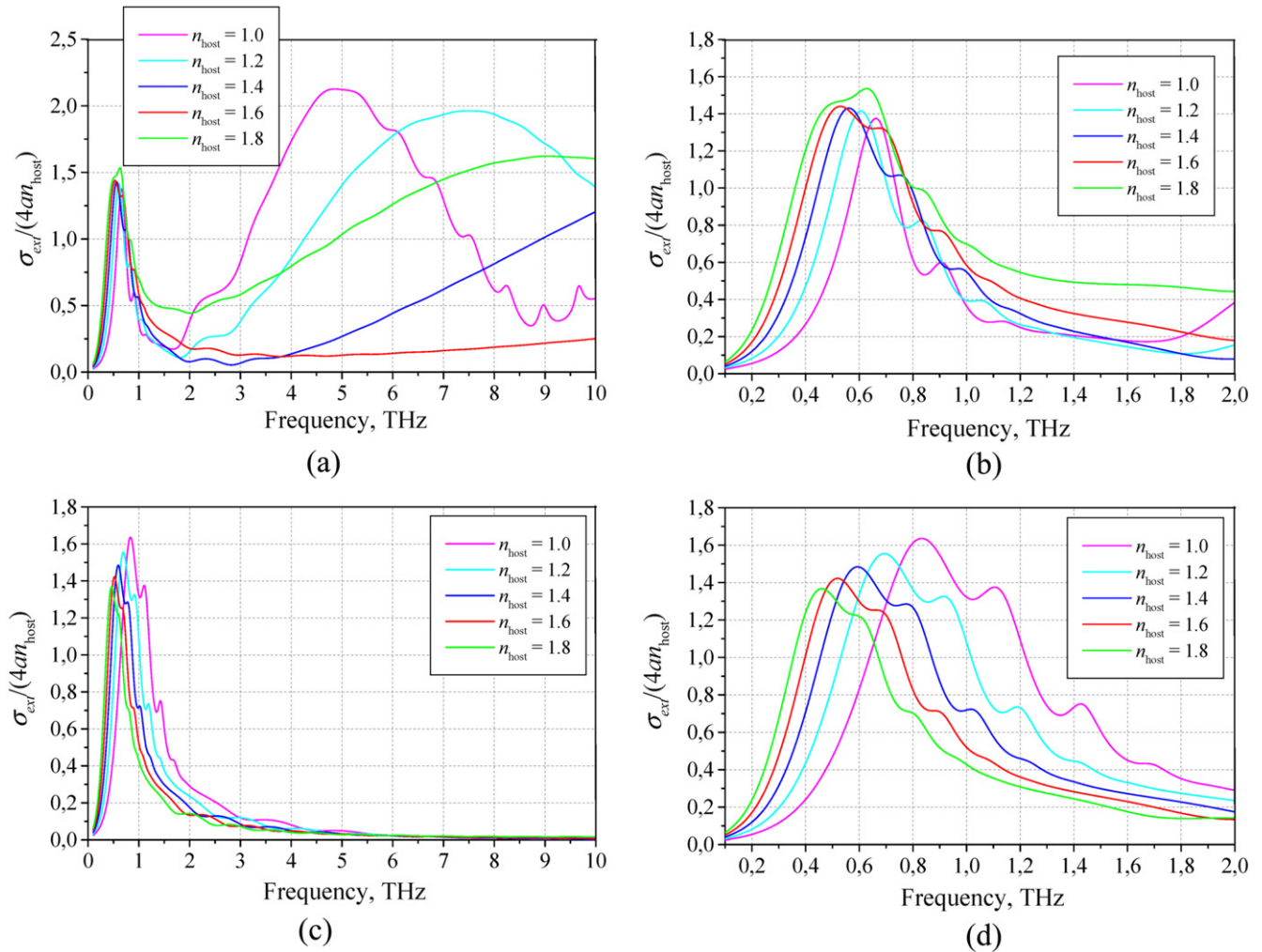

Figure 11. The spectra of the normalized ECS for different values of the host-medium refractive index n_{host}. The dielectric tube of the dielectric permittivity $\varepsilon_c = 2.4$ with a graphene cover has (a), (b) $b/a = 0.5$, (c), (d) 0.99. Panels (b), (d) are zooms of the lower-frequency parts of panels (a), (c), respectively. Here, $\mu_c = 0.25$ eV, and the other parameters are the same as in figure 8.
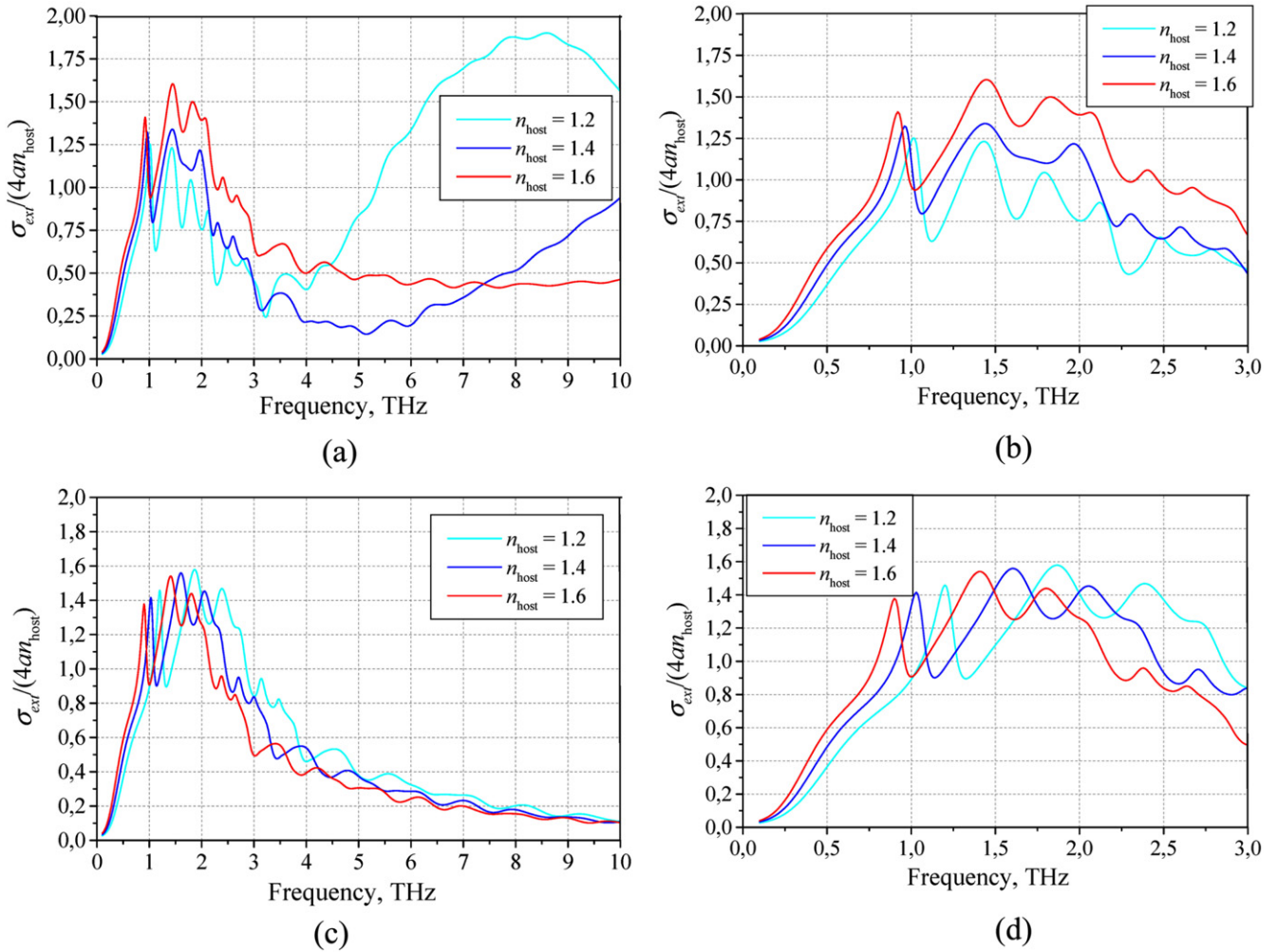
Figure 12. The spectra of the normalized ECS for different values of the host-medium refractive index n_{host}. The dielectric tube of the permittivity $\varepsilon_c = 2.4$ with a graphene cover has (a), (b) $\mu_c = 1.0$ eV and $b/a = 0.5$, (c), (d) 0.99. Panels (b), (d) are zooms of the lower-frequency parts of panels (a), (c), respectively.
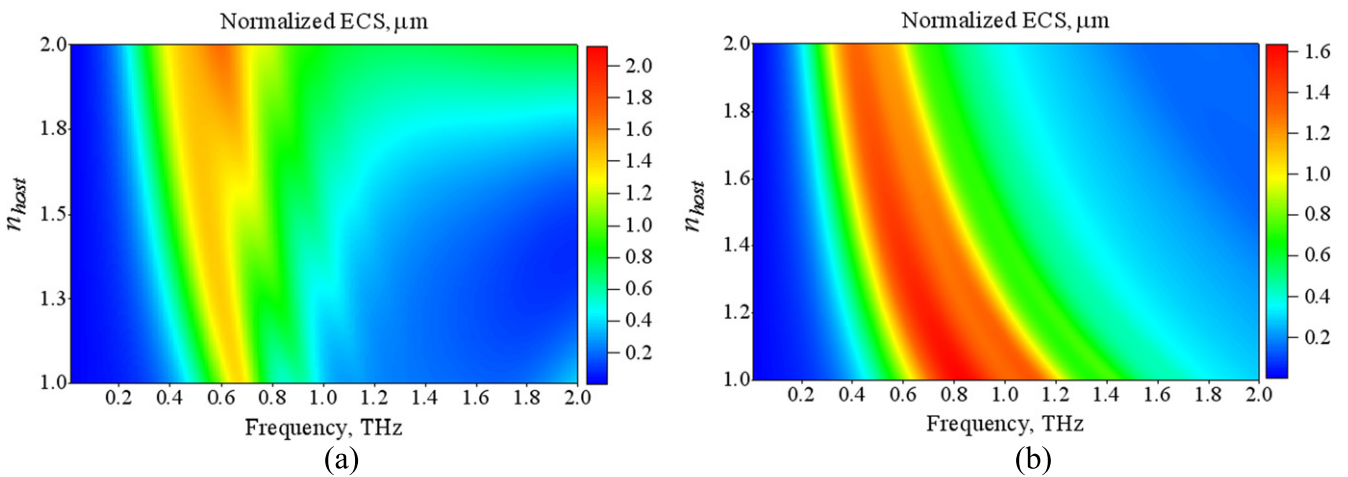

Figure 13. The maps of the normalized ECS as a function of the frequency and the host-medium refractive index for a circular dielectric tube covered with a graphene layer with (a) $b/a = 0.5$, (b) 0.99 placed into a medium with a varying refractive index. The tube parameters are the same as in figure 9.

Table 1. Refractive-index sensitivity and FOM of the plasmon resonances on a graphene-covered dielectric tube.

	b/a	S_{bulk}, μm/RIU	FWHM, μm	FOM
$\mu_c = 0.25$ eV	0.0	99.2	443.3	0.224
	0.5	185.4	441.0	0.415
	0.9	328.2	469.4	0.744
	0.99	410.0	332.8	0.874
$\mu_c = 1.0$ eV	0.0	8.8	332.8	0.026
	0.5	72.6	297.9	0.244
	0.9	192.2	293.9	0.654
	0.99	208.2	274.4	0.758

advantages of the thin-walled tube configuration over the thick-walled one in terms of a much larger sensitivity to the changes in n_{host}.

6. Bulk refractive-index sensitivities and FOM values

In applications, there are two most important engineering characteristics of optical or THz-wave range sensors of the refractive-index change: the sensitivity and the FOM [12–15]. Using the obtained numerical results, we calculated the bulk refractive-index sensitivity as $S_{\text{bulk}} = \Delta\lambda_{\text{res}}^{\text{LSP}}/\Delta n_{\text{host}}$, which corresponded to the resonance wavelength shift $\Delta\lambda_{\text{res}}^{\text{LSP}}$ of the first LSP resonance obtained under the refractive-index variation Δn_{host}. The FOM was defined as FOM = S_{bulk}/FWHM, where FWHM is the full width at half maximum of the peak at the fixed value of n_{host}. Assuming that $n_{\text{host}} = 1.4$, which corresponds to the water solutions of the most typical biological substances, we calculated these quantities for several different values of the ratio b/a. The results are presented in table 1. It can be added that the peaks on the spectral dependences of the ECS are not perfectly symmetric, which can suggest their fitting with Fano-shaped formulas, instead of Lorentz-shaped ones. However, we found that even the simplified evaluation, neglecting the asymmetry, was able to deliver reasonable information.

As one can see, the values of both sensitivity and FOM associated with the first LSP-mode resonance on a graphene-covered dielectric microtube grow up if the tube gets thinner. This could be expected, of course, as, in this case, the LSP-mode field has a larger overlap with the host medium. Still, the substrate is a necessary component of a graphene-based sensor. Our results demonstrate that, for the realistic values of substrate thickness and material, the sensitivity of the first LSP resonance of a graphene-covered dielectric rod is of the same order as reported previously for the flat-strip graphene sensors [4]. However, for a thin tube (say, with $a/b = 0.99$), they can be two to three times higher, depending on the value of the chemical potential. This can be related to the fact that we computed the microsized graphene-covered tubes, while, in [4], the graphene strips were assumed to be nanosized. This change in the wavelength range appears to be important. In the sub-THz range, the graphene is moderately less lossy than

in the high-THz range and significantly less lossy than the noble metals in the optical range. The results obtained support the proposition of using a thin-wall graphene-covered microtube as a sensor for the changes in the bulk refractive index of the host medium. They also agree with a recent study of a microsize flat graphene strip as a THz-range plasmon resonator used for the sensing of refractive index [25].

7. Conclusions

We studied, using the accurate analytical-numerical method, the scattering and absorption of the H-polarized plane wave by a microsized circular dielectric cylinder and a microsized circular dielectric tube covered with a graphene cover. This study has revealed that such composite scatterers are quite complicated open resonators, which support several types of resonances. One of them is the resonances of the graphene cover explained by the excitation of the LSP-mode standing waves, and the other is associated with the conventional modes of the circular dielectric scatterer, which acquires the properties of WGM resonances if the circular boundary has an optical length exceeding several wavelengths in the object material. For the sensing, the former resonances are promising, while the latter are unwanted and can be removed from the working range of frequencies by making the tube supporting graphene cover as thin as possible. The tunability of graphene enables one to manipulate with the LSP-mode resonances.

The sensitivity and FOM of a tube-based resonance sensing structure, in the THz range, are high enough to consider it as a possible microsized sensor of the refractive-index changes in the host medium.

References

[1] Gusynin V P, Sharapov S G and Carbotte J P 2007 Magnetooptical conductivity in graphene *J. Phys.: Condens. Matter* **19** 026222

[2] Jablan M, Buljan H and Soljacic M 2009 Plasmonics in graphene at infrared frequencies *Phys. Rev.* B **80** 245435

[3] Thongrattanasiri S, Koppens F H L and Garcia de Abajo F J 2012 Complete optical absorption in periodically patterned graphene *Phys. Rev. Lett.* **108** 047401–5

[4] Vasic B, Isic G and Gajic R 2013 Localized surface plasmon resonances in graphene ribbon arrays for sensing of dielectric environment at infrared frequencies *J. Appl. Phys.* **113** 113110

[5] Shapoval O V, Gomez-Diaz J S, Perruisseau-Carrier J, Mosig J and Nosich A I 2013 Integral equation analysis of plane wave scattering by coplanar graphene-strip gratings in the THz range *IEEE Trans. Terahertz Sci. Techn.* **3** 666–73

[6] Balaban M V, Shapoval O V and Nosich A I 2013 THz wave scattering by a graphene strip and a disk in the free space: integral equation analysis and surface plasmon resonances *J. Opt.* **15** 114007

[7] Low T and Avouris P 2014 Graphene plasmonics for terahertz to mid-infrared applications *ACS Nano* **8** 1086–101

[8] Zinenko T L 2015 Scattering and absorption of terahertz waves by a free-standing infinite grating of graphene strips: analytical regularization analysis *J. Opt.* **17** 055604

[9] Zhao J, Liu X, Qiu W, Ma Y, Huang Y, Wang J-X, Qiang K and Pan J-Q 2014 Surface-plasmon-polariton whispering-gallery mode analysis of the graphene monolayer coated InGaAs nanowire cavity *Opt. Express* **22** 5754–61

[10] Xiao T-H, Gan L and Li Z-Y 2015 Graphene surface plasmon polaritons transport on curved substrates *Photon. Res.* **3** 300–7

[11] Riso M, Cuevas M and Depine R A 2015 Tunable plasmonic enhancement of light scattering and absorption in graphene coated subwavelength wires *J. Opt.* **17** 075001

[12] Homola J 2008 Surface plasmon resonance sensors for detection of chemical and biological species *Chem. Rev.* **108** 462–93

[13] McPhillips J, Murphy A, Jonsson M P, Hendren W R, Atkinson R, Hook F, Zayats A V and Pollard R J 2010 High-performance biosensing using arrays of plasmonic nanotubes *ACS Nano* **4** 2210–6

[14] Murphy A, Sonnefraud Y, Krasavin A V, Ginzburg P, Morgan F, McPhillips J, Wurtz G, Maier S A, Zayats A V and Pollard R 2013 Fabrication and optical properties of large-scale arrays of gold nanocavities based on rod-in-a-tube coaxials *Appl. Phys. Lett.* **102** 103103

[15] Velichko E A and Nosich A I 2013 Refractive-index sensitivities of hybrid surface-plasmon resonances for a core–shell circular silver nanotube sensor *Opt. Lett.* **38** 4978–81

[16] Velichko E A 2014 Plasmon resonances in the scattering and absorption of light by a circular gold nanotube *Proc. Int. Conf. Electronics and Nanotechnology (ELNANO-2014) (Kiev)* pp 42–5

[17] Hower G L, Olsen R G, Earls J D and Schneider J B 1993 Inaccuracies in numerical calculations of scattering near natural frequencies of penetrable objects *IEEE Trans. Antennas Propag.* **41** 982–6

[18] Boriskin A V, Boriskina S V, Rolland A, Sauleau R and Nosich A I 2008 Test of the FDTD accuracy in the analysis of the scattering resonances associated with high-Q whispering-gallery modes of a circular cylinder *J. Opt. Soc. Am.* A **25** 1169–73

[19] Niegemann J, Pernice W and Busch K 2009 Simulation of optical resonators using DGTD and FDTD *J. Opt. A: Pure Appl. Opt.* **11** 114015

[20] Hanson G W 2008 Dyadic Green's functions for an anisotropic, non-local model of biased graphene *IEEE Trans. Antennas Propag.* **56** 747–57

[21] Strutt J W (Lord Rayleigh) 1881 On the electromagnetic theory of light *Philos. Mag.* **12** 81–101

[22] Wait J R 1986 *Introduction to Antennas and Propagation* (London: Peter Peregrinus)

[23] Smotrova E I, Benson T M, Sewell P, Ctyroky J and Nosich A I 2008 Lasing frequencies and thresholds of the dipole-type supermodes in an active microdisk concentrically coupled with a passive microring *J. Opt. Soc. Am.* A **25** 2884–92

[24] Smotrova E I, Nosich A I, Benson T M and Sewell P 2006 Ultralow lasing thresholds of the pi-type supermodes in cyclic photonic molecules composed of sub-micron disks with monopole and dipole modes *IEEE Photonics Technol. Lett.* **18** 1993–5

[25] Shapoval O V and Nosich A I 2016 Bulk refractive-index sensitivities of the THz-range plasmon resonances on a micro-size graphene strip *J. Phys. D: Appl. Phys.* **49** 055105